magnetochemistry

MDPI

Article

S-Functionalized Tripods with Monomethylene Spacers: Routes to Tetrairon(III) Single-Molecule Magnets with Ultrashort Tethering Groups

Andrea Cornia [1,*], Chiara Danieli [1], Fabio Meglioli [1], Erik Tancini [1,2], Alessio Nicolini [1,2], Maria Jesus Rodriguez-Douton [1,†], Anne-Laure Barra [3], Marco Affronte [2] and Roberta Sessoli [4]

1 Department of Chemical and Geological Sciences, University of Modena and Reggio Emilia & INSTM, I-41125 Modena, Italy; chiarad635@gmail.com (C.D.); fabiomeglio88@gmail.com (F.M.); erik.tancini@gmail.com (E.T.); alessio.nicolini@unimore.it (A.N.); maria.douton@nano.cnr.it (M.J.R.-D.)
2 Department of Physics, Informatics, and Mathematics, University of Modena and Reggio Emilia, I-41125 Modena, Italy; marco.affronte@unimore.it
3 Laboratoire National des Champs Magnétiques Intenses-CNRS, Univ. Grenoble-Alpes, CEDEX 9, F-38042 Grenoble, France; anne-laure.barra@lncmi.cnrs.fr
4 Department of Chemistry 'Ugo Schiff', University of Florence & INSTM, I-50019 Sesto Fiorentino (FI), Italy; roberta.sessoli@unifi.it
* Correspondence: acornia@unimore.it; Tel.: +39-059-205-8645
† Present address: NEST, Nanoscience Institute-CNR, I-56127 Pisa, Italy.

Received: 29 September 2020; Accepted: 28 October 2020; Published: 30 October 2020

Abstract: The organization of single-molecule magnets (SMMs) on surfaces is a mainstream research path in molecular magnetism. Of special importance is the control of grafting geometry in chemisorbed monolayers on metal surfaces. We herein present the synthesis, solid-state structure, and magnetic characterization of propeller-like tetrairon(III) SMMs containing the shortest-reported tethering groups for gold surfaces. Functionalization of molecular structure is attained using 2-R-2-(hydroxymethyl)propane-1,3-diol tripodal proligands (H_3L^R). The R substituents comprise a *mono*methylene spacer and three different terminations known to act as stable precursors of S-Au bonds (R = CH_2SCN, CH_2SAc and CH_2SS*n*Bu). These chemical groups are shown to be chemically compatible with the tetrairon(III) core and to afford fully-functional SMMs in crystalline form and in fair to excellent yields.

Keywords: single-molecule magnets; iron; ligand design; chemisorption; EPR spectroscopy

1. Introduction

The design of molecules exhibiting a directionally bistable magnetic moment, known as single-molecule magnets (SMMs), has made tremendous progress in the last few years, with operating temperatures that now approach 80 K in some dysprosocenium derivatives [1]. A parallel research path is the investigation of SMMs processed into thin films, down to single layers or even isolated molecules deposited on surfaces. Advances in this field are also significant and demonstrate that SMMs have a real application potential in high-density information storage and molecular spintronics [2–5].

Although uncompetitive with the best SMMs in terms of working temperature, propeller-like tetrairon(III) complexes were pivotal to show that SMMs can maintain their memory effect on a surface [6–8]. In most reported cases, these small polynuclear complexes with an $S = 5$ ground state are assembled using 2-R-2-(hydroxymethyl)propane-1,3-diol tripodal proligands (H_3L^R) and have the formula $[Fe_4(L^R)_2(dpm)_6]$, where Hdpm is 2,2,6,6-tetramethylheptane-3,5-dione (also known as dipivaloylmethane). A vast pool of tripods was synthesized that allowed to shape and functionalize

these structures with chiral, photoresponsive, redox-active, and metal-coordinating R groups [9]. Such a possibility was also widely exploited to promote and control adsorption on surfaces. For instance, the derivative with R = H has a discoidal shape and physisorbs on hexagonal boron nitride/Rh(111) [10] and graphene/Ir(111) [11,12] with the magnetic easy axis perpendicular to the surface, affording highly ordered monolayers. Bulkier substituents, like R = Ph [8] and CH_2SMe [13], trigger a tilted physisorption geometry on Au(111) and Pb(111), respectively, and form less ordered monolayers.

Chemisorbed monolayers on gold were prepared introducing S-based "alligator clips" in the structure of Fe_4 complexes [14]. To this aim, thioacetyl-terminated alkyl chains of different length were primarily used, like R = $(CH_2)_3SAc$ [15,16], $(CH_2)_5SAc$ [6,17], and $(CH_2)_9SAc$ [7,14,18]. The monoester of pentaerythritol (R = CH_2OH) with (±)-α-lipoic acid was also used to anchor molecules on gold through the 1,2-dithiolan-3-yl moiety. This cyclic disulphide does not react with the tetrairon(III) core but its S-S linkage spontaneously splits at gold surfaces with the formation of two covalent Au-S bonds [19,20]. An interesting outcome of these studies was that shorter tethers like R = $(CH_2)_3SAc$ [15] and $(CH_2)_5SAc$ [6] promote a partially oriented grafting of the molecules.

As a follow-up, this paper presents synthetic routes to $[Fe_4(L^R)_2(dpm)_6]$ complexes functionalized with ultrashort tethers: R = CH_2SCN (**1**), CH_2SAc (**2**) and CH_2SS*n*Bu (**3**). In all these derivatives R consists of a *mono*methylene spacer and a terminal group acting as a stable precursor for S-Au bond, namely SCN [21,22], SAc [23–25] and SSR′ [26,27]. Four crystalline phases (**1**, **2**·Et_2O, **2**·0.375Et_2O and **3**) were isolated and studied by single-crystal X-ray diffraction, direct current (DC) and alternating current (AC) magnetic measurements and high frequency electron paramagnetic resonance (HF-EPR) spectroscopy. The investigation demonstrated that the above functionalities are chemically compatible with the tetrairon(III) core and that the resulting complexes behave as SMMs.

2. Results and Discussion

2.1. Synthesis

Three new derivatives of 2-(hydroxymethyl)propane-1,3-diol (H_3L^R) were prepared in this study (Scheme 1). The reaction of 2-(bromomethyl)-2-(hydroxymethyl)propane-1,3-diol (**4**) with excess potassium thiocyanate in acetonitrile under reflux gave the corresponding thiocyanate ($H_3L^{CH_2SCN}$) in essentially quantitative yield (Scheme 1a). The procedure customarily used to prepare tripodal proligands functionalized with thioacetyl-terminated alkyl chains is base-catalyzed Tollens condensation [28,29] between the appropriate unsaturated aldehyde and formaldehyde, followed by the addition of thioacetic acid promoted by 2,2′-azobisisobutyronitrile (AIBN) [14,30]. With this approach, the shortest accessible alkyl spacer is a *di*methylene chain.

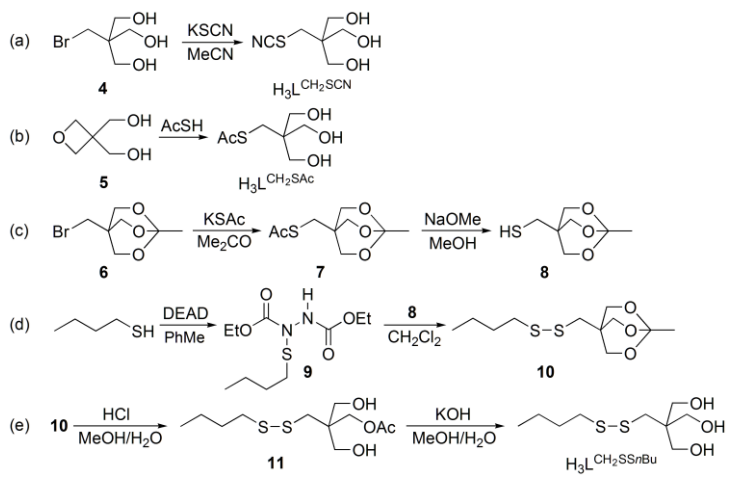

Scheme 1. Synthesis of tripodal proligands H_3L^R (DEAD is diethyl azodicarboxylate).

We found that the $H_3L^{CH_2SAc}$ proligand could be very conveniently synthesized from (oxetane-3,3-diyl)dimethanol (**5**) and thioacetic acid in a solvent-free ring-opening reaction similar to that reported for 3,3-dimethyloxetane (Scheme 1b) [31]. The third tripodal proligand, $H_3L^{CH_2SSnBu}$, features a disulfide moiety for direct covalent grafting to a Au surface. The length of the terminal chain, a *n*-butyl group, was chosen to enhance the solubility of the proligand in nonpolar or moderately polar solvents while still permitting good crystal packing. The study involved a careful scrutiny of available methods for the synthesis of asymmetric disulfides. Very low yields were obtained by air oxidation of mixtures of thioacetate **7**, prepared from bromide **6**, and *S*-*n*-butyl thioacetate in the presence of NaOMe/MeOH, due to the extensive formation of symmetric disulfides [32]. Among methods with reportedly enhanced chemoselectivity [33,34], use of diethyl azodicarboxylate (DEAD) adducts gave the best results. As shown in Scheme 1c–e addition product **9** was prepared in good yield by treating DEAD with butane-1-thiol in toluene at 25 °C [34], low temperatures being in this case unnecessary [35,36]. The reaction of **9** with thiol **8**, produced by deprotection of **7** with NaOMe/MeOH, gave the desired compound in 73% yield after acid hydrolysis of orthoacetate **10** and final saponification of monoester **11** to liberate the triol moiety.

Tetrairon(III) complexes were synthesized from $[Fe_4(OMe)_6(dpm)_6]$ [37] and an excess of the appropriate proligand in diethyl ether, according to Equation (1):

$$[Fe_4(OMe)_6(dpm)_6] + 2H_3L^R \rightarrow [Fe_4(L^R)_2(dpm)_6] + 6\ MeOH. \quad (1)$$

Although $H_3L^{CH_2SCN}$ and $H_3L^{CH_2SAc}$ are only poorly soluble in diethyl ether, the reaction proceeds smoothly with all proligands used. Slow solvent evaporation directly afforded the products as X-ray quality crystals, except for **3**, which was recrystallized from 1,2-dimethoxyethane (DME). In their IR spectra, complexes **1** and **2** show C≡N and C=O stretching bands at 2153 and 1701 cm^{-1}, respectively, which indicate that thiocyanate and thioacetyl groups are incorporated intact in the structures. This conclusion is supported by the single-crystal X-ray diffraction data presented in the next Section.

2.2. Structural Descriptions

The structure of tetrairon(III) molecules in these compounds was determined by single-crystal X-ray diffraction at low temperature (120–140 K; see Table S1). At room temperature, the prismatic crystals of **1** are rhombohedral, with unit cell parameters similar to those of the R = Me derivative [37], suggesting a disordered SCN group; however, at 120 K the structure is monoclinic (space group *C*2/*c*) and the asymmetric unit contains half tetrairon(III) complex. The two thiocyanate groups are symmetry-related by a two-fold axis and are directed roughly perpendicular to the molecular plane (Figure 1).

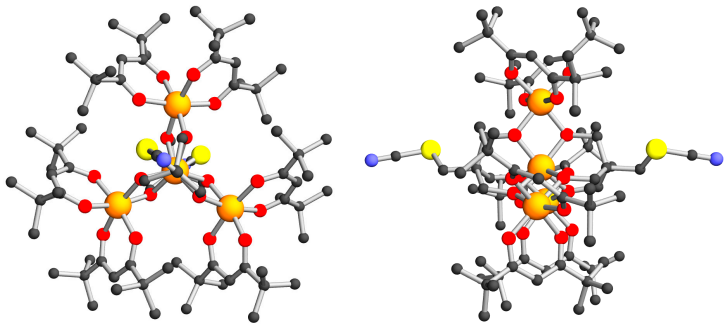

(**a**) (**b**)

Figure 1. Molecular structure of **1** viewed along (**a**) and perpendicular to (**b**) the idealized three-fold axis. Color code: C = black, N = blue, O = red, S = yellow, Fe = orange. Minority components of disordered *t*Bu groups and hydrogen atoms have been omitted.

Turning now to **2**, two different crystalline phases, both belonging to triclinic space group $P\bar{1}$, were found to occur in erratic proportions in crystallization batches. These two phases are solvatomorphs of **2** and show a markedly different propensity to lose crystallinity when removed from their mother solution. The first phase is a mono(diethyl ether) solvate (**2**·Et_2O) and grows as platelets which rapidly lose crystallinity upon standing in air, presumably due to loss of diethyl ether from the lattice. The asymmetric unit contains two Fe_4 molecules (MOL1 and MOL2) and two diethyl ether molecules (the structure of MOL1 and MOL2 is displayed in Figure 2 and Figure S1, respectively). The second phase (**2**·0.375Et_2O) grows as block-like crystals which exhibit much greater air-stability as compared with **2**·Et_2O. Two Fe_4 molecules (MOL3 and MOL4) and 0.75 diethyl ether molecules are present in the asymmetric unit (see Figures S2 and S3).

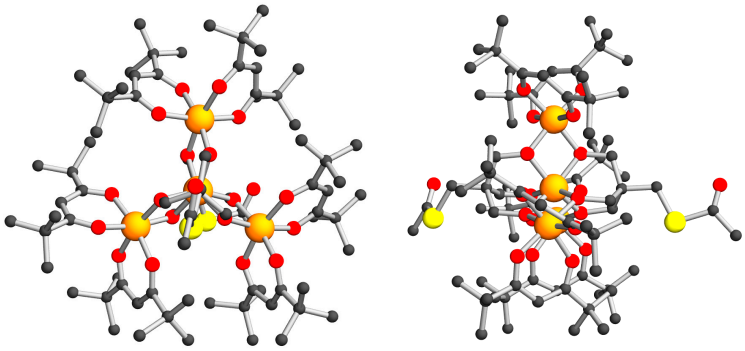

(**a**) (**b**)

Figure 2. Molecular structure of MOL1 in **2**·Et_2O viewed along (**a**) and perpendicular to (**b**) the idealized three-fold axis. Same color code as in Figure 1. Minority components of disordered *t*Bu groups and hydrogen atoms have been omitted.

Two crystal phases were also isolated for complex **3**. Structural data were collected on well-diffracting prisms, which contain the unsolvated complex and belong to monoclinic space group *C*2/*c*. However, **3** was also obtained as extensively twinned air-stable square blocks which analyze well for unsolvated **3**, but whose diffraction pattern escaped indexing. The two crystal phases likely represent polymorphs of **3**. In the structurally characterized crystal phase, the asymmetric unit consists in half tetrairon(III) complex and molecules have crystallographically imposed two-fold symmetry, as in **1** (Figure 3). All tetrairon(III) complexes reported in this study have at least one disordered *t*Bu group in the solid state; disorder also affects one or both R groups in MOL2 and MOL4 of **2**·*x*Et_2O and in **3**.

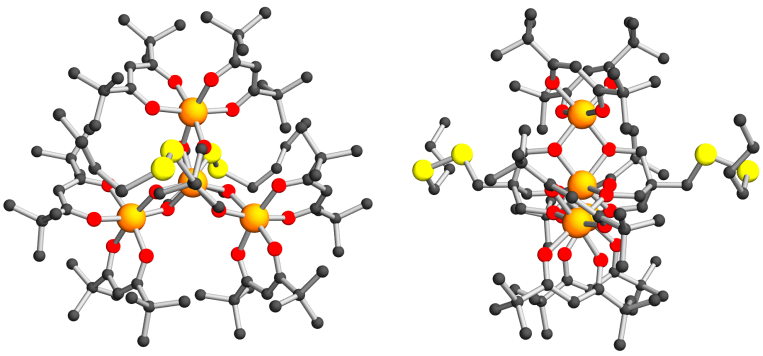

(**a**) (**b**)

Figure 3. Molecular structure of **3** viewed along (**a**) and perpendicular to (**b**) the idealized three-fold axis. Same color code as in Figure 1. Minority components of disordered moieties and hydrogen atoms have been omitted.

Our structural investigations directly prove that the newly synthesized S-functionalized tripods can be successfully incorporated in propeller-like tetrairon(III) cores. The analyzed crystal phases belong to monoclinic or triclinic space groups and the crystallographic molecular symmetry is thus low: C_2 in **1** and **3** (two-fold axis passing through the central metal and one of the peripheral metals), and C_1 in both solvatomorphs of **2**. However, if the R substituents are disregarded, molecular structures approach three-fold symmetry quite closely; it is thus meaningful to use the angular parameters θ and φ, associated with the trigonally distorted coordination sphere of the central ion, and the helical pitch γ (see [38] for definitions). The resulting values are presented in Table S2, along with those of the derivative with R = CH_2SMe (**12**) [13], and are typical for propeller-like tetrairon(III) complexes [9].

Except for thiocyanate derivative in **1**, all used tripodal ligands exhibit a remarkable conformational flexibility in the solid state, which may contribute to explaining why (pseudo)polymorphs are often encountered. The top views provided in Figure 1a, Figure 2a, Figure 3a and Figures S1a–S3a, show that the S-C bond with the *mono*methylene spacer tends to adopt a staggered conformation with respect to the coordinated tripodal function. However, because of the approximately three-fold local symmetry, the relative arrangement of the two S-C bonds within the same molecule varies considerably. For instance, it is *syn* in MOL1 and MOL3 of **2**·$x$$Et_2O$ (Figure 2a and Figure S2a, respectively) but *anti* in **1** (Figure 1a). The four crystallographically independent molecules in **2**·$x$$Et_2O$ further differ in the conformation of the thioacetyl groups, as resulting from rotation around the S-C bond with the *mono*methylene spacer. The planar SAc groups can range from being roughly perpendicular to the molecular plane to forming a dihedral angle (δ) down to about 30° with it; in this case, they approach van der Waals contact with *t*Bu groups of dpm^- ligands. In MOL1 and MOL3 of **2**·$x$$Et_2O$, for instance, both thioacetyl groups are ordered within experimental resolution. However, while in MOL1 one thioacetyl has δ = 85.7° and the second one has δ = 30.1° (Figure 2b), in MOL3 both thioacetyls display a perpendicular arrangement with δ = 88.7° and 89.9° (Figure S2b). In MOL2 and MOL4 the situation is more complicated, since one or both side chains are disordered. MOL2 (Figure S1b) features one ordered (δ = 81.2°) and one disordered thioacetyl (about 59:41 with δ = 29.2 and 31.1°, respectively). In MOL4 (Figure S3b) one side chain is disordered over two positions (about 69:31 with δ = 52.0 and 83.8°, respectively) while the second one is detectably split over three positions (about 44:31:25 with δ = 38.2, 83.8 and 33.5°, respectively).

Finally, it is important to notice that these propeller-like molecules can exist as Δ and Λ isomers; however, they crystallize in centrosymmetric space groups and are, thus, isolated as racemic mixtures.

2.3. DC Magnetic Studies

The magnetic properties of vacuum-treated powder samples of **1**, **2**·Et_2O and **3** were studied in DC mode by recording low-field $\chi_M T$ vs. T and isothermal M_M vs. H data, where χ_M and M_M are molar magnetic susceptibility and molar magnetization, respectively. Here we describe the results obtained for **1**, which is representative of the whole series. Data for the remaining compounds are available in Figures S4 and S5. The temperature dependence of the $\chi_M T$ product for **1** shows the trend typical of antiferromagnetically coupled systems with uncompensated spin moments (Figure 4). The presence of dominant antiferromagnetic interactions is clearly revealed by the room-temperature $\chi_M T$ value, which is significantly lower than expected for four uncoupled s_i = 5/2 spins (17.5 emu K mol^{-1} with g = 2.00). On decreasing temperature the curve features a minimum at around 100–110 K, then rises again up to a maximum, which is close to the value of the Curie constant for an S = 5 total spin ground state (C = 15.0 emu K mol^{-1} with g = 2.00). $\chi_M T$ vs. T data at T > 20 K were then fitted to a Heisenberg-Dirac-Van Vleck *plus* Zeeman Hamiltonian, assuming three-fold symmetry and using two different superexchange-coupling constants to describe nearest-neighbor (J_1) and next-nearest-neighbor (J_2) interactions within the "J" convention (Equation (2)):

$$\hat{H} = J_1(\hat{\mathbf{s}}_1\cdot\hat{\mathbf{s}}_2+\hat{\mathbf{s}}_1\cdot\hat{\mathbf{s}}_3+\hat{\mathbf{s}}_1\cdot\hat{\mathbf{s}}_4) + J_2(\hat{\mathbf{s}}_2\cdot\hat{\mathbf{s}}_3+\hat{\mathbf{s}}_3\cdot\hat{\mathbf{s}}_4+\hat{\mathbf{s}}_2\cdot\hat{\mathbf{s}}_4) + \mu_B g\hat{\mathbf{S}}\cdot\mathbf{B} \quad (2)$$

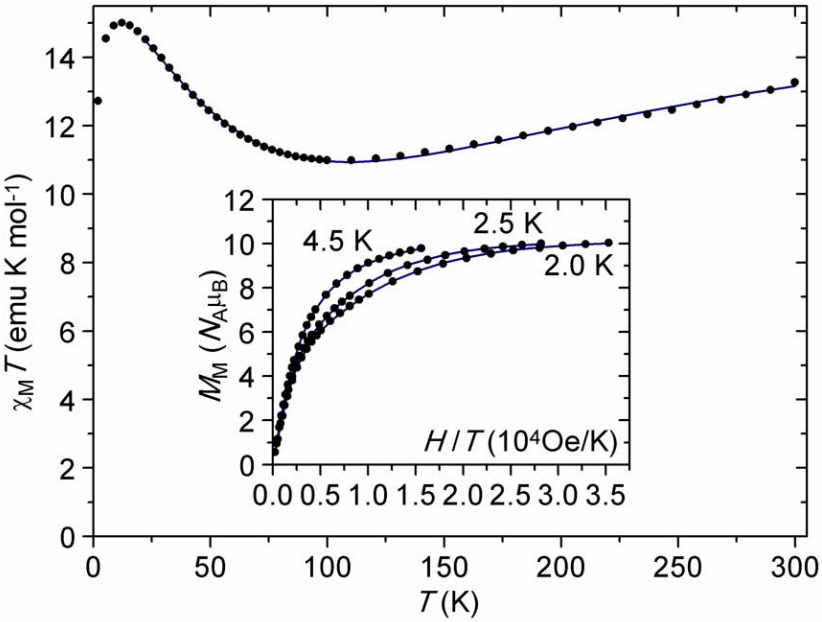

Figure 4. Temperature dependence of the molar magnetic susceptibility in low field, and molar magnetization isotherms at low temperature (inset) for **1**. Solid lines represent the best-fit curves.

($\mathbf{s}_1$ denotes the spin vector on the central ion). The J_1, J_2 and g values obtained with this procedure are gathered in Table 1 along with those of **12** [13] for comparison. J_1 is invariably antiferromagnetic and typical in magnitude for this class of tetrairon(III) SMMs [9], whereas J_2 is zero within the fitting error or slightly ferromagnetic. However, the best-fit value of J_2 must be regarded with care since this parameter may compensate for systematic errors in data collection and reduction [14,39]. Isothermal M_M vs. H data recorded at low temperature show pronounced nesting when plotted as a function of H/T (Figure 4, inset), indicating the presence of magnetic anisotropy acting on the ground spin state. We thus fitted the data using the S = 5 Giant-Spin (GS) Hamiltonian in Equation (3):

$$\hat{H}_{GS} = \mu_B \hat{\mathbf{S}} \cdot \bar{\bar{\mathbf{g}}} \cdot \mathbf{B} + D\left[\hat{S}_z^2 - S(S+1)/3\right] + E\left(\hat{S}_x^2 - \hat{S}_y^2\right) + B_4^0 \hat{O}_4^0 \quad (3)$$

retaining only second-order axial anisotropy ($E = B_4^0 = 0$) and assuming an isotropic g-factor ($\bar{\bar{\mathbf{g}}} = g\bar{\bar{\mathbf{I}}}$ with $\bar{\bar{\mathbf{I}}}$ = identity matrix). The best-fit parameters so obtained are gathered in Table 1 along with those of **12** [13] for comparison.

Table 1. Magnetic parameters for **1**, **2**·Et_2O, **3,** and **12**.

Compound	1	2·Et_2O	3	12 [1]
J_1 (cm^{-1}), J_2 (cm^{-1}) [2]	15.69(8), −0.03(6)	15.800(16), −0.121(14)	14.36(7), −0.19(6)	14.64(8), −0.12(7) [3]
g [2]	2.008(3)	2.0057(6)	1.972(3)	2.000(3) [3]
g, D (cm^{-1}) [4]	2.0545(12), −0.3961(18)	2.021(2), −0.426(3)	1.978(3), −0.419(3)	2.013(2), −0.423(3)
a_2 [4,5]	−0.0547(8)	−0.0236(12)	−0.0666(13)	−0.0548(10)
$g_x = g_y$, g_z [6]	2.00(1), 2.00(1)	1.995(10), 2.00(1)	not available	2.00(1), 2.001(5)
D (cm^{-1}) [6]	−0.412(1)	−0.438(2)	not available	−0.430(1)
E (cm^{-1}), B_4^0 (cm^{-1}) [6]	0.010(2), 1.6(3)·10^{-5}	0.009(4), 1.5(3)·10^{-5}	not available	0.041(2), 1.2(1)·10^{-5}
U_{eff}/k_B (K), [7] U/k_B (K) [8]	14.48(7), 14.8	16.32(5), 15.8	16.22(10), 15.1	13.78(8), 15.5
τ_0 (s) [7]	3.15(7)·10^{-7}	4.87(10)·10^{-7}	3.63(15)·10^{-7}	5.2(2)·10^{-7}

[1] Data from [13], unless otherwise noted. [2] From low-field $\chi_M T$ vs. T data at T > 20 K. [3] In [13] a different model was used to extract J_1, J_2 and g. [4] From isothermal M_M vs. H data at low T. [5] Preferential orientation correction (see Experimental Section). [6] From HF-EPR spectra. [7] From AC susceptibility data at H_{DC} = 1 kOe. [8] Calculated as $(|D|/k_B)S^2$ (preferably from the HF-EPR D value, when available).

2.4. HF-EPR Spectra

The powder HF-EPR spectra of **1** and **2**·Et_2O were recorded from 5 to 20 K at 190 and 230 GHz. Figure 5 displays the data for **1** at 230 GHz, while the remaining spectra are provided as Figures S6–S8. At low temperature, the spectra exhibit the characteristic features for systems with a high-spin ground state associated to a quasi-axial Ising-type anisotropy: the parallel transitions are observed in the low-field part of the spectrum (i.e., below the $g = 2$ resonance position) whereas the perpendicular transitions appear in the high-field part. On decreasing temperature, the signals at the extremes of the spectrum get stronger and stronger as expected for transitions corresponding to $M_S = -5 \rightarrow -4$ (Figure 5). Moving towards the center of the spectrum, the successive $\Delta M_S = 1$ transitions are observed. The unequal spacing of neighboring transitions in the parallel region is the signature of higher-order axial anisotropy terms. The simulated spectra (Figure 5 and Figures S6–S8 were obtained with the GS Hamiltonian in Equation (3) and the resulting best-fit parameters are gathered in Table 1. Molar magnetization isotherms simulated with these parameters are presented in Figure S9 for **1** and **2** Et_2O.

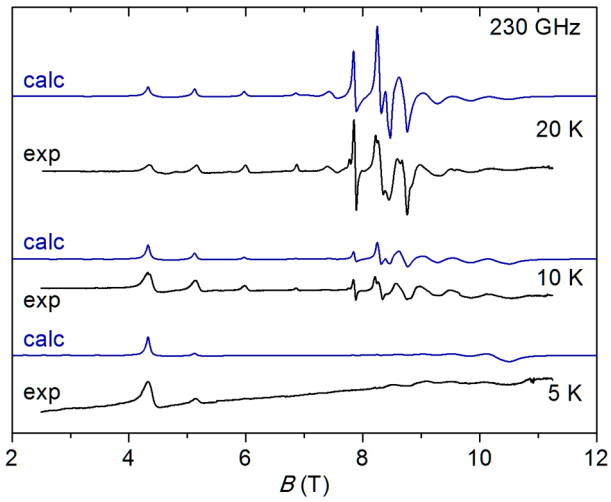

Figure 5. Experimental (exp) and calculated (calc) HF-EPR spectra of **1** at 230 GHz and different temperatures.

In spite of their low crystallographic molecular symmetry, compounds **1** and **2**·Et_2O have almost perfectly axial anisotropy in their $S = 5$ ground state. The value of $|D/E| \sim 0.02$ is about four times smaller than in related compound **12** [13], whose spin-Hamiltonian parameters are also reported in Table 1. A quasi-axial, Ising-type anisotropy with $|D| = 0.40 \div 0.45$ cm^{-1} in the ground spin state is characteristic for this class of tetrairon(III) SMMs featuring two coordinated tripodal ligands [9]. The observed anisotropy is primarily determined by single-ion terms (with the dominant contribution provided by peripheral Fe^{3+} ions) and, to a lesser extent, by spin-spin interaction anisotropy [39]. Typical is also the positive fourth-order axial parameter B_4^0, whereby the 11 sublevels of the $S = 5$ manifold define a "compressed" parabola [37,38].

An accurate reproduction of the spectra required an anisotropic linewidth (i.e., a different linewidth when the applied field is directed along x, y or z). In addition, while the linewidth of z-transitions remains essentially constant across the whole spectrum, with only minor differences between **1**, **2**·Et_2O, and **12**, x- and y-transitions behave differently. Their linewidth increases significantly when going from the center to the extremes of the spectrum. Furthermore, such a linewidth variation is largest for **1,** intermediate for **2**·Et_2O, and smallest for **12** (Table S3). This suggests the occurrence of a compound-dependent distribution of spin-Hamiltonian parameters in the same material (strain effects), affecting primarily the E value.

2.5. AC Magnetic Studies

We investigated the dynamics of the magnetization on the same powder samples by means of AC susceptibility measurements. A small static field (H_{DC} = 1 kOe) was applied in order to slow down under-barrier relaxation by quantum tunneling while only marginally affecting spin levels, thereby allowing to measure a larger set of relaxation times [13]. The appearance of maxima in the out-of-phase component of the molar magnetic susceptibility (χ_M'') is a clear signature of slow magnetic relaxation (Figure 6). We thus fitted the χ_M'' vs. frequency (ν) curves to an extended Debye model [40,41] to extract the average relaxation time τ, the width of the distribution of relaxation times α, and $\chi_{M,T} - \chi_{M,S}$ as functions of temperature ($\chi_{M,T}$ and $\chi_{M,S}$ are the isothermal and adiabatic molar magnetic susceptibilities, respectively). The results are gathered in Tables S4–S6. As shown in Figure 6, linear ln(τ) vs. 1/T plots are obtained indicating thermally activated relaxation mechanisms, whereby the relaxation time follows Arrhenius law $\tau = \tau_0 \exp[U_{eff}/(k_B T)]$. The effective energy barrier U_{eff} within the series of compounds **1**, **2**·Et_2O and **3** (Table 1) is comparable to the total splitting of the S = 5 multiplet, evaluated as $(|D|/k_B)S^2$, showing that in the adopted experimental conditions under-barrier relaxation is largely suppressed. The fastest-relaxing species is **1**, which also features the smallest $|D|$ according to both M_M vs. H data and (when available) HF-EPR spectra. In compound **12** [13] the effective barrier is instead significantly lower than $(|D|/k_B)S^2$. This is likely to arise from the large rhombicity of **12**, whose E parameter is four times larger than in **1** and **2**·Et_2O. As a result, under-barrier relaxation is enhanced [38], and **12** attains a very similar spin dynamics to **1**.

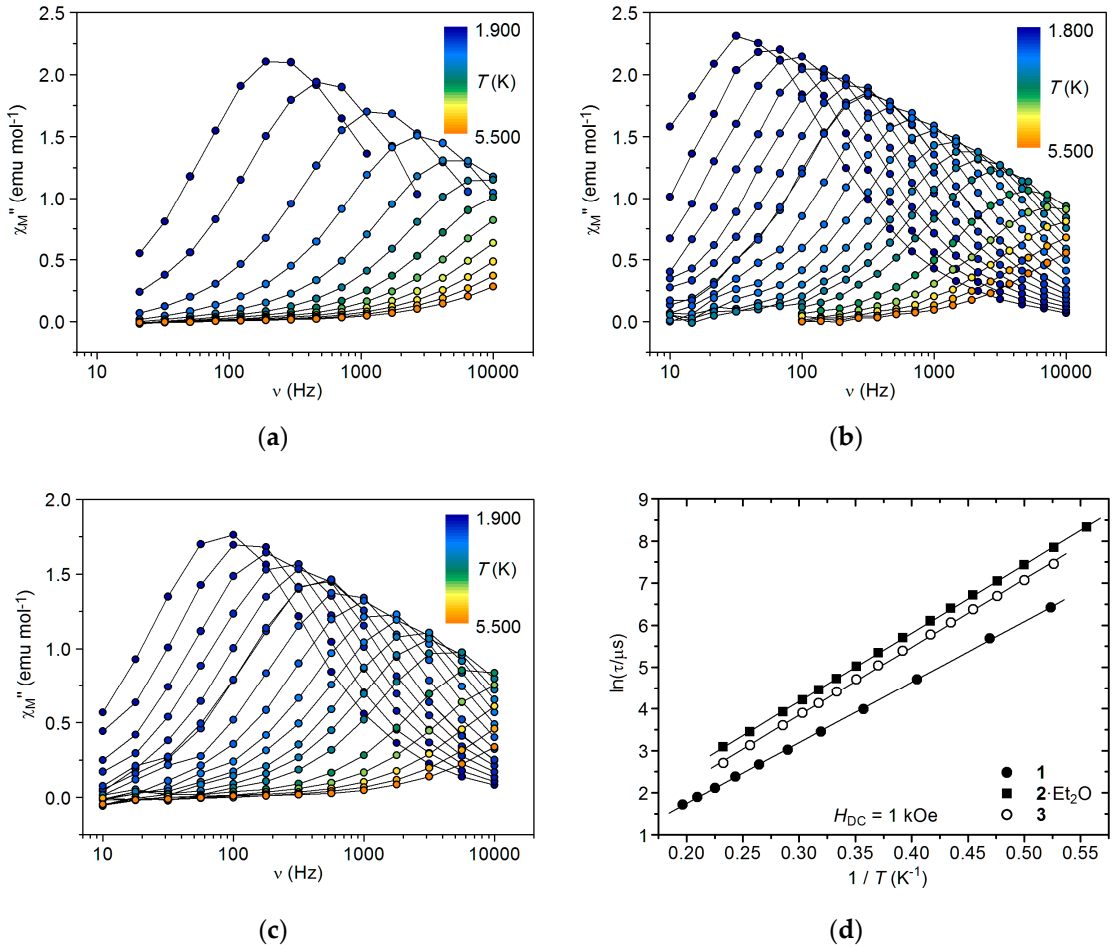

Figure 6. Frequency dependence of the out-of-phase molar magnetic susceptibility at H_{DC} = 1 kOe for **1** (**a**), **2**·Et_2O (**b**), and **3** (**c**). Panel (**d**) shows Arrhenius plots for the three compounds, as obtained from τ vs. T data at H_{DC} = 1 kOe.

The α parameter in **1**, **2**·Et_2O, and **3** is 0.16–0.21 at the lowest temperatures reached and decreases upon heating (Figure S10), indicating that the distribution of relaxation times narrows with increasing temperature. These α values and their temperature dependence are in agreement with literature data on similar tetrairon(III) compounds [42,43]. Differences between **1** and **2**·Et_2O are within the experimental error, notwithstanding the narrower distribution of spin-Hamiltonian parameters in the latter (Table S3). The α value in **12** is, instead, significantly smaller at all temperatures (Figure S10). Rewardingly, this compound also exhibits the smallest EPR linewidth variation in the series and, by consequence, the narrowest distribution of spin-Hamiltonian parameters (Table S3).

3. Experimental Section

3.1. Materials and Methods

All reactants and solvents were reagent grade and used without further purification, unless otherwise stated. Anhydrous solvents were either of commercial origin (dichloromethane, toluene) or prepared by standard methods [44]. Diethyl ether, from a freshly opened can, was pre-dried by stirring overnight with granular $CaCl_2$, refluxed over Na/benzophenone and distilled under N_2. Methanol and DME were refluxed over $Mg(OMe)_2$ and NaH, respectively; acetone was dried over $CaSO_4$, while acetonitrile was sequentially dried with 3A molecular sieves and CaH_2; these solvents were finally distilled with protection against moisture prior to use. Petroleum ether was the fraction with boiling point 40–60 °C. (Oxetane-3,3-diyl)dimethanol (**5**) was prepared in 79% yield by following a literature method [45], except that the crude product was purified by column chromatography (silica gel, CH_2Cl_2:MeOH 4:1). 4-(Bromomethyl)-1-methyl-2,6,7-trioxabicyclo[2.2.2]octane (**6**) was prepared as described elsewhere [46]. KSCN was dried in vacuum over P_2O_5 prior to use. NaOMe was used as a solution in methanol, prepared by careful addition of metallic Na to anhydrous methanol under N_2 atmosphere. $[Fe_4(OMe)_6(dpm)_6]$ was prepared as described in [37]. Thin-layer chromatography (TLC) was performed on silica gel glass plates 60 F_{254} from Merck KGaA (Darmstadt, Germany). Compounds were visualized under an UV lamp and/or using I_2 or ceric ammonium molybdate stains. Elemental analysis was carried out on an EA1110 CHNS-O automatic analyzer from CE Instruments (Milan, Italy). ^{1}H NMR spectra were recorded at 303 K and 200.13 MHz with an FT-DPX200 NMR spectrometer from Bruker Spectrospin Italiana S.r.l. (Milan, Italy); ^{13}C NMR spectra were recorded at 303 K and 100.61 MHz with an FT-NMR AVANCE400 spectrometer from Bruker BioSpin S.r.l. (Milan, Italy); chemical shifts are expressed in ppm downfield from external tetramethylsilane, by setting the residual ^{1}H signal of acetone-d_6, CD_3OD, CD_2Cl_2 and $CDCl_3$ at 2.05, 3.31, 5.32, and 7.26 ppm, respectively, and the methyl ^{13}C signal of acetone-d_6 at 29.84 ppm [47]; coupling constants (J) are given in hertz. The following abbreviations are used in reporting NMR data: s = singlet, brs = broad singlet, d = doublet, t = triplet, q = quartet, m = multiplet. IR spectra were recorded as KBr pellets or on NaCl disks using an FTIR-4200 spectrophotometer with 2 cm^{-1} resolution from Jasco Corporation (Tokyo, Japan); $\widetilde{\nu}_{max}$ values are given in cm^{-1}. The following abbreviations are used in reporting IR data: s = strong, m = medium, w = weak, br = broad.

3.2. Synthesis of 3-hydroxy-2,2-bis(hydroxymethyl)propyl thiocyanate ($H_3L^{CH_2SCN}$)

2-(Bromomethyl)-2-(hydroxymethyl)propane-1,3-diol (**4**) (1.095 g, 5.501 mmol) and KSCN (1.61 g, 16.6 mmol) were refluxed in dry acetonitrile (5 mL) under N_2 until complete conversion (about 70 h). The suspension was allowed to cool down to room temperature and treated with a mixture of chloroform and acetonitrile (2:1 *v*/*v*, 45 mL). The precipitated inorganic salts were filtered off, the solution was dried over $MgSO_4$, and the solvent was removed under reduced pressure to give an almost colorless oil (1.23 g). Purification by column chromatography (silica gel, Me_2CO:$CHCl_3$:MeOH 16:15:1 *v*/*v*) gave the product as a dense colorless oil which solidified upon standing (0.923 g, 95%). R_f = 0.31 (silica gel, Me_2CO:$CHCl_3$ 1:1 *v*/*v*). ^{1}H NMR (acetone-d_6): 3.92 (3H, t, ^3J = 5.0, OH), 3.64 (6H, d, ^3J = 5.0, CH_2O),

3.33 (2H, s, CH_2S). IR (NaCl disk): 3398 (br, s, OH), 2939 (m, CH), 2886 (m, CH), 2156 (s, SCN), 1467 (m), 1415 (m), 1310 (m), 1094 (m), 1037 (s, C-O), 878 (m), 839 (m).

3.3. Synthesis of S-[3-hydroxy-2,2-bis(hydroxymethyl)propyl] ethanethioate ($H_3L^{CH_2SAc}$)

A 10-mL round-bottomed flask equipped with a reflux condenser topped with a $CaCl_2$ drying tube was charged with **5** (1.008 g, 8.530 mmol) and thioacetic acid (1.84 mL, 25.7 mmol). The reaction mixture was immersed for a few minutes in an oil bath preheated at 35 °C, then heated to 60 °C and stirred at this temperature for 5 h, following the reaction by TLC. The crude product was purified by column chromatography (silica gel, CH_2Cl_2:MeOH 4:1 *v*/*v*) to give the product as a dense yellow oil (1.115 g, 67%). R_f = 0.53 (silica gel, CH_2Cl_2:MeOH 4:1 *v*/*v*). ^{1}H NMR (CD_3OD): 3.51 (6H, s, CH_2O), 3.04 (2H, s, CH_2S), 2.34 (3H, s, CH_3).

*3.4. Synthesis of S-[(1-methyl-2,6,7-trioxabicyclo[2.2.2]octan-4-yl)methyl] ethanethioate (**7**)*

Orthoacetate **6** (1.556 g, 6.976 mmol) was dissolved in anhydrous acetone (13 mL) under N_2. Potassium thioacetate (0.984 g, 8.62 mmol) was added, then the mixture was stirred and heated to reflux under N_2 for 1.5 h. The solid was filtered off on a G4 frit and the solvent evaporated under vacuum to give crude **7** as a brown oil (1.588 g), which was used without further purification. R_f = 0.41 (silica gel, CH_2Cl_2:MeOH 100:1 *v*/*v*). ^{1}H NMR (acetone-d_6): 3.89 (6H, s, CH_2O), 2.86 (2H, s, CH_2S), 2.37 (3H, s, CH_3CO), 1.28 (3H, s, $CH_3C(O)_3$).

*3.5. Synthesis of (1-methyl-2,6,7-trioxabicyclo[2.2.2]octan-4-yl)methanethiol (**8**)*

Anhydrous methanol (14 mL) and NaOMe (2.994 M solution in MeOH, 28 µL, 0.084 mmol) were mixed in a two-neck round-bottomed flask and refluxed under N_2. Thioacetate **7** (370 mg, 1.70 mmol) was added and reflux was continued for 1.5 h. The solvent was then removed by evaporation under vacuum avoiding exposure to air. The product was used without further purification. R_f = 0.48 (silica gel, CH_2Cl_2:MeOH 100:1 *v*/*v*).

*3.6. Synthesis of diethyl 1-(butylsulfanyl)hydrazine-1,2-dicarboxylate (**9**)*

DEAD (40% in toluene, stored over 4A molecular sieves, 9.93 g, 22.8 mmol) was introduced in a flame-dried round-bottomed flask kept under N_2. Butane-1-thiol (2.06 g, 22.8 mmol) dissolved in anhydrous toluene (2 mL) was added dropwise to the stirred DEAD solution over a 45′ period. Upon further stirring at room temperature for 4 h, the solution turned progressively from orange to pale yellow and a white precipitate formed. Petroleum ether (25 mL) was added, the solution was cooled in an ice bath and filtered on a G3 frit. Evaporation of the solvent at reduced pressure gave crude **9** (5.76 g) which was purified by column chromatography (silica gel, petroleum ether:EtOAc, gradient 6:1 to 3:1 *v*/*v*) to give **9** as a pale yellow oil (4.51 g, 75%). R_f = 0.44 (silica gel, petroleum ether:EtOAc 2:1 *v*/*v*). ^{1}H NMR ($CDCl_3$): 6.97 (1H, brs, NH), 4.23 (2H, q, ^3J = 7.1, CH_2O), 4.20 (2H, q, ^3J = 7.1, CH_2O), 2.98 (2H, t, ^3J = 7.2, CH_2S), 1.63 (2H, m, CH_2CH_2S), 1.44 (2H, m, $CH_3CH_2CH_2$), 1.29 (3H, t, ^3J = 7.1, CH_3CH_2O), 1.27 (3H, t, ^3J = 7.1, CH_3CH_2O), 0.91 (3H, t, ^3J = 7.2, $CH_3CH_2CH_2$). Spectra comparable to those reported in [35].

3.7. Synthesis of 2-[(butyldisulfanyl)methyl]-2-(hydroxymethyl)propane-1,3-diol ($H_3L^{CH_2SSnBu}$)

Anhydrous dichloromethane (5 mL) and a solution of **9** (446 mg, 1.69 mmol) in the same solvent (5 mL) where sequentially added to **8** (1.70 mmol), prepared as described above. The mixture was left stirring under N_2 atmosphere and the formation of disulfide **10** was monitored by TLC (R_f = 0.59 on silica gel, petroleum ether:EtOAc 2:1 *v*/*v*). After 4 h the solvent was completely removed under vacuum and methanol (20 mL) and HCl (3 M in MeOH, 250 µL) were added so as to promote the acid-catalyzed opening of orthoacetate moiety to give monoacetate **11**, as confirmed by TLC. Aqueous KOH (0.98 M, 1 mL) was finally added to liberate the triol function. The clear orange solution was dried under vacuum

and the crude product (725 mg) was purified by column chromatography (silica gel, CH_2Cl_2:MeOH, gradient from 19:1 to 14:1 *v*/*v*) to give the product as a pale orange oil which solidified upon prolonged standing (297 mg, 73% yield). R_f = 0.11 (silica gel, CH_2Cl_2:MeOH 19:1 *v*/*v*). ^{1}H NMR (CD_3OD): 3.59 (6H, s, CH_2O), 2.96 (2H, s, SCH_2C^{IV}), 2.73 (2H, t, ^3J = 7.2, CH_2CH_2S), 1.68 (2H, m, CH_2CH_2S), 1.44 (2H, m, CH_3CH_2), 0.94 (3H, t, ^3J = 7.2, CH_3). ^{1}H NMR (acetone-d_6): 3.73 (brs, OH), 3.63 (6H, s, CH_2O), 3.03 (2H, s, SCH_2C^{IV}), 2.75 (2H, t, ^3J = 7.3, CH_2CH_2S), 1.67 (2H, m, CH_2CH_2S), 1.42 (2H, m, CH_3CH_2), 0.92 (3H, t, ^3J = 7.3, CH_3). ^{13}C NMR (acetone-d_6): 64.16 (CH_2O), 46.60 (C^{IV}), 43.26 (SCH_2C^{IV}), 38.73 (CH_2CH_2S), 31.83 (CH_2CH_2S), 22.19 (CH_3CH_2), 13.94 (CH_3). IR (NaCl disk): 3375 (br, s, OH), 2957 (s, CH), 2929 (s, CH), 2873 (m, CH), 1464 (m), 1432 (m), 1413 (m), 1379 (m), 1302 (w), 1273 (w), 1220 (w), 1085 (m), 1032 (s, C-O), 879 (w), 826 (w), 622 (w).

*3.8. Synthesis of [$Fe_4(L^{CH_2SCN})_2(dpm)_6$] (**1**)*

[$Fe_4(OMe)_6(dpm)_6$] (60.3 mg, 0.0400 mmol) and $H_3L^{CH_2SCN}$ (19.1 mg, 0.108 mmol) were stirred overnight in anhydrous diethyl ether (25 mL). The filtered solution was slowly concentrated at room temperature over a dry methanol trap (40 mL) to give orange-red crystals which were washed with the vapor diffusion mixture and dried in vacuum (61 mg, 91%). Anal. calcd (%) for $C_{78}H_{130}Fe_4O_{18}N_2S_2$: C 56.05, H 7.84, N 1.68, S 3.84; found: C 55.76, H 7.61, N 1.70, S 3.62. IR (KBr pellet): 2962 (s, CH), 2954 (s, CH), 2929 (m, CH), 2903 (m, CH), 2872 (m, CH), 2843 (m, CH), 2153 (m, SCN), 1596 (m), 1576 (s), 1565 (s), 1552 (s), 1538 (s), 1506 (s), 1456 (w), 1401 (s), 1383 (s), 1357 (s), 1304 (w), 1293 (w), 1248 (m), 1228 (m), 1198 (w), 1179 (m), 1144 (m), 1128 (m), 1064 (m), 1025 (w), 963 (w), 936 (w), 873 (m), 846 (w), 821 (w), 804 (w), 796 (m), 765 (w), 738 (w), 692 (w), 653 (w), 622 (m), 568 (s), 502 (m), 479 (m).

*3.9. Synthesis of [$Fe_4(L^{CH_2SAc})_2(dpm)_6$]·x$Et_2O$ (**2**·xEt_2O)*

[$Fe_4(OMe)_6(dpm)_6$] (0.0600 g, 0.0398 mmol) was dissolved in anhydrous diethyl ether (25 mL) with stirring, a solution of $H_3L^{CH_2SAc}$ (0.0479 g, 0.246 mmol) in the same solvent (2 mL) was added and the resulting mixture was stirred for 1 h. Slow concentration of the clear solution at room temperature over a dry methanol trap (40 mL) afforded dark-orange crystals (**2**·Et_2O and **2**·0.375Et_2O in erratic proportions). The crystals were collected by filtration, washed with the vapour diffusion mixture, then with anhydrous methanol until colorless washings and finally dried in vacuum, which causes complete solvent loss from the lattice (0.0599 g, 88%). All characterization data, except for single-crystal X-ray diffraction data, were collected on vacuum-dried crystallization batches containing predominantly **2**·Et_2O. Anal. calcd (%) for $C_{80}H_{136}Fe_4O_{20}S_2$: C 56.34, H 8.04, S 3.76; found: C 56.46, H 8.06, S 3.72. IR (KBr pellet): 2963 (s, CH), 2867 (s, CH), 1701 (m, C=O), 1592 (s), 1564 (s), 1548 (s), 1535 (s), 1505 (s), 1451 (w), 1400 (s), 1383 (s), 1357 (s), 1291 (w), 1247 (m), 1227 (m), 1178 (m), 1144 (m), 1122 (m), 1059 (m), 956 (w), 872 (m), 805 (w), 792 (m), 759 (m), 739 (w), 624 (m).

*3.10. Synthesis of [$Fe_4(L^{CH_2SSnBu})_2(dpm)_6$] (**3**)*

$H_3L^{CH_2SSnBu}$ (27.1 mg, 0.113 mmol) dissolved in anhydrous diethyl ether (3 mL) was added to a solution of [$Fe_4(OMe)_6(dpm)_6$] (56.9 mg, 0.0377 mmol) in the same solvent (23 mL). After 24 h stirring the solution was filtered and the solvent slowly evaporated in air at room temperature. The resulting partially crystalline solid was redissolved in anhydrous DME (5 mL) and the filtered solution was slowly evaporated almost to dryness over a dodecane trap. The dark-orange crystals were washed with a MeOH:DME mixture (10:1 *v*/*v*) to remove liquid residuals and dried under vacuum (40.1 mg, 59%). Crystallization batches comprise well-diffracting prisms and/or highly-twinned square blocks. All characterization data, except for single-crystal X-ray diffraction data, were collected on samples containing predominantly the latter crystal phase. Anal. calcd (%) for $C_{84}H_{148}Fe_4O_{18}S_4$: C 56.12, H 8.30, S 7.13; found: C 56.36, H 8.19, S 7.07. ^{1}H NMR (CD_2Cl_2): 10.5 (very brs, *t*Bu), 1.05 (brs), −13 (very brs, -CH=). IR (KBr pellet): 2962 (s, CH), 2929 (m, CH), 2905 (m, CH), 2871 (m, CH), 1592 (s), 1577 (s), 1564 (s), 1548 (s), 1535 (s), 1505 (s), 1452 (w), 1399 (s), 1382 (s), 1357 (s), 1291 (w), 1246 (m),

1227 (m), 1177 (m), 1144 (m), 1122 (m), 1059 (m), 963 (w), 872 (m), 805 (w), 792 (m), 759 (w), 739 (w), 621 (m), 569 (m), 500 (w).

3.11. Single-Crystal X-ray Diffraction

All structures were analyzed with a four-circle X8APEX diffractometer from Bruker-Nonius (Delft, The Netherlands) equipped with Mo-Kα radiation (0.71073 Å) and a Kryo-Flex N_2 flow cryostat for data collection at 120(2) or 140(2) K. The structures were solved by direct methods using the SIR92 program [48]. Full- or block matrix least-squares refinement on ${F_o}^2$ was performed with the SHELXL-97 or SHELXL-2014/7 programs [49], implemented in the WINGX suite [50]. Disorder effects on *t*Bu groups, on the side chains of tripodal ligands and on lattice solvent were handled by introducing constraints/restraints on geometry and/or displacement parameters [51]. Hydrogen atoms were set in idealized positions with isotropic displacement parameters constrained to those of the attached carbon atoms. Crystal data and refinement parameters, and further refinement details are available in Table S1 and Supplementary Note 1, respectively. Graphics utilized Ortep-3 for Windows (v2.0) [50] and POV-Ray™ for Windows (v3.5) [52]. CCDC 2033840-2033843 contain the supplementary crystallographic data for this paper and can be obtained free of charge via www.ccdc.cam.ac.uk/data_request/cif, or by emailing data_request@ccdc.cam.ac.uk, or by contacting The Cambridge Crystallographic Data Centre, 12 Union Road, Cambridge CB2 1EZ, UK; fax: +44 1223 336033.

3.12. Magnetic Measurements

Magnetic data in DC and AC mode were recorded on MPMS and PPMS instruments from Quantum Design GmbH (Darmstadt, Germany). We used vacuum-treated powder samples of **1**, **2**·Et_2O and **3** with masses of 22.19, 10.77, and 12.33 mg, respectively. Samples were either pressed in a pellet and wrapped in Teflon® tape (**2**·Et_2O and **3**) or restrained in eicosane (**1**). DC data were recorded at temperatures ranging from T = 1.8–2.0 to 300 K and in fields H = 1 kOe (T < 35 K) or 10 kOe ($T \geq 35$ K). The M_M/H ratio, where M_M is the molar magnetization, was assumed to correspond to the static molar magnetic susceptibility χ_M. Isothermal magnetization curves were also recorded in fields up to 50–70 kOe at 1.8–2.0, 2.5 and 4.5 K. Raw data, after correction for the sample holder and addenda, were reduced using molecular weights of 1671.4 (**1**), 1705.5 (**2**) and 1797.7 (**3**) and diamagnetic corrections (estimated from Pascal's constants [53]) of −940 (**1**), −957 (**2**) and −1050 (**3**)·10^{-6} emu mol^{-1}. AC magnetic data in a 1 kOe applied static field (H_{DC}) were recorded on the same samples at frequencies of the oscillating field (1–10 Oe) from 10 Hz to 10 kHz and at temperatures between 1.8–1.9 and 5.5 K. The fitting of DC magnetic data was carried out using original software based on F02ABF and E04FCF NAG routines for matrix diagonalization and least-squares fitting, respectively [54]. The modelling of preferential orientation effects, i.e., a non-perfectly random distribution of crystallite orientations in the sample, was required for an accurate fitting of M_M vs. H curves. To this aim, we used the correction scheme recently published by some of us, which implies the refinement of one additional least-squares parameter (a_2) [16]. The estimated standard deviations of best-fit parameters, quoted in Table 1, were calculated from the variances of the regression coefficients, as provided by routine E04YCF [54].

3.13. HF-EPR Spectra

HF-EPR spectra were recorded on vacuum-treated powder samples, using a home-made spectrometer operating in single-pass configuration at T ranging from 5 to 20 K and in applied magnetic fields up to 12 T. Gunn diode sources operating at either 95 or 115 GHz associated to frequency doublers were used to produce microwaves at 190 or 230 GHz for sample excitation. To avoid field-induced orientation effects, the samples were pressed into pellets. Powder spectra were simulated using a dedicated software, after an initial fitting of the resonance positions [55,56].

Since it was not possible to introduce simultaneously an anisotropic linewidth and a strain, each spectrum was obtained as the sum of several component spectra. Each component spectrum involved

only part of the transitions for which an anisotropic linewidth was considered; the sum of these component spectra allowed considering all the possible transitions (see Table S3 for the details on the linewidths used).

4. Conclusions

Synthetic routes were devised to 2-R-2-(hydroxymethyl)propane-1,3-diol derivatives with R = CH_2SCN, CH_2SAc and CH_2SS*n*Bu. The tripods were subsequently used to functionalize propeller-like tetrairon(III) SMMs by a ligand-exchange reaction. The products were obtained in crystalline form and in fair to excellent yields; according to crystallographic, spectroscopic and chemical evidence they contain intact S-based groups. Magnetic studies and HF-EPR spectroscopy showed that the new complexes retain the magnetic properties typical of SMMs of this family (S = 5, $|D| = 0.41 \div 0.44$ cm^{-1}, U_{eff}/k_B = 14–16 K).

The R substituents described in this paper are known precursors for S-Au bonds [21–27]. They are thus expected to promote chemisorption of Fe_4 molecules on gold surfaces, whereas more "innocent" substituents like R = H [10–12], Ph [8] and CH_2SMe [13] afford physisorbed monolayers. In addition, the ultrashort alkyl tethers should restrain adsorption geometry, resulting in oriented monolayers. Efforts are now underway to study the interaction of these new tetrairon(III) derivatives with gold surfaces.

Supplementary Materials: The following are available online at http://www.mdpi.com/2312-7481/6/4/55/s1; Supplementary Note 1: Structure refinement details for **1**, **2**·Et_2O, **2**·0.375Et_2O and **3**; Figure S1. Molecular structure of MOL2 in **2**·Et_2O viewed along and perpendicular to the idealized three-fold axis; Figure S2. Molecular structure of MOL3 in **2**·0.375Et_2O viewed along and perpendicular to the idealized three-fold axis; Figure S3. Molecular structure of MOL4 in **2**·0.375Et_2O viewed along and perpendicular to the idealized three-fold axis; Figure S4. Temperature dependence of the molar magnetic susceptibility in low field, and molar magnetization isotherms at low temperature for **2**·Et_2O; Figure S5. Temperature dependence of the molar magnetic susceptibility in low field, and molar magnetization isotherms at low temperature for **3**; Figure S6. Temperature dependent HF-EPR spectra of **1** at 190 GHz along with best simulations; Figure S7. Temperature dependent HF-EPR spectra of **2**·Et_2O at 190 GHz along with best simulations; Figure S8. Temperature dependent HF-EPR spectra of **2**·Et_2O at 230 GHz along with best simulations; Figure S9. Molar magnetization isotherms recorded on **1** and **2**·Et_2O compared with calculated curves based on HF-EPR parameters in Table 1; Figure S10. Temperature dependence of the α parameter in a 0.1 T applied static field for **1**, **2**·Et_2O, **3** and **12**; Table S1. Crystal data and refinement parameters for **1**, **2**·Et_2O, **2**·0.375Et_2O and **3**; Table S2. Geometrical parameters for the coordination sphere of the central iron ion in **1**, **2**·Et_2O, **2**·0.375Et_2O, **3** and **12**, after averaging according to D_3 symmetry; Table S3. Linewidths (in Gauss) used to simulate HF-EPR spectra for compounds **1**, **2**·Et_2O, and **12**, depending on the transition ($M \rightarrow M'$) and on magnetic field orientation (x, y or z); Table S4. Fitting parameters of the isothermal χ_M'' vs. ν curves (H_{DC} = 1 kOe) based on the extended Debye model for compound **1**; Table S5. Fitting parameters of the isothermal χ_M'' vs. ν curves (H_{DC} = 1 kOe) based on the extended Debye model for compound **2**·Et_2O; Table S6. Fitting parameters of the isothermal χ_M'' vs. ν curves (H_{DC} = 1 kOe) based on the extended Debye model for compound **3**.

Author Contributions: Conceptualization: A.C.; methodology: A.C., C.D., and M.J.R.-D.; software: A.C.; validation: A.C. and R.S.; formal analysis: A.C., F.M., E.T., and A.-L.B.; investigation: A.C., C.D., F.M., E.T., A.N., M.J.R.-D., A.-L.B., M.A., and R.S.; resources: C.D., F.M., E.T., and M.J.R.-D.; data curation: A.C.; writing—original draft preparation: A.C.; writing—review and editing: A.C. and R.S.; visualization: A.C. and A.-L.B.; supervision: A.C.; project administration: A.C.; funding acquisition: A.C. and R.S. All authors have read and agreed to the published version of the manuscript.

Funding: This research was funded by European Union through Network of Excellence MAGMANET, grant number 15767, NanoSci-ERA project SMMTRANS, grant number 06NSE03, and ERC Advanced Grant MolNanoMaS, grant number 267746, to R.S.; it was also supported by Italian MIUR through a PRIN2008 project, grant number 2008FZK5AC.

Conflicts of Interest: The authors declare no conflict of interest.

References

1. Guo, F.-S.; Day, B.M.; Chen, Y.-C.; Tong, M.-L.; Mansikkamäki, A.; Layfield, R.A. Magnetic hysteresis up to 80 kelvin in a dysprosium metallocene single-molecule magnet. *Science* **2018**, *362*, 1400–1403. [CrossRef] [PubMed]
2. Cornia, A.; Talham, D.R.; Affronte, M. Thin Layers of Molecular Magnets. In *Molecular Magnetic Materials: Concepts and Applications*; Sieklucka, B., Pinkowicz, D., Eds.; Wiley-VCH: Weinheim, Germany, 2017; pp. 187–229. ISBN 9783527694228.
3. Krylov, D.S.; Schimmel, S.; Dubrovin, V.; Liu, F.; Nguyen, T.T.N.; Spree, L.; Chen, C.-H.; Velkos, G.; Bulbucan, C.; Westerström, R.; et al. Substrate-Independent Magnetic Bistability in Monolayers of the Single-Molecule Magnet $Dy_2ScN@C_{80}$ on Metals and Insulators. *Angew. Chem. Int. Ed.* **2020**, *59*, 5756–5764. [CrossRef] [PubMed]
4. Studniarek, M.; Wäckerlin, C.; Singha, A.; Baltic, R.; Diller, K.; Donati, F.; Rusponi, S.; Brune, H.; Lan, Y.; Klyatskaya, S.; et al. Understanding the Superior Stability of Single-Molecule Magnets on an Oxide Film. *Adv. Sci.* **2019**, *6*, 1901736. [CrossRef] [PubMed]
5. Ara, F.; Oka, H.; Sainoo, Y.; Katoh, K.; Yamashita, M.; Komeda, T. Spin properties of single-molecule magnet of double-decker Tb(III)-phthalocyanine ($TbPc_2$) on ferromagnetic Co film characterized by spin polarized STM (SP-STM). *J. Appl. Phys.* **2019**, *125*, 183901. [CrossRef]
6. Mannini, M.; Pineider, F.; Danieli, C.; Totti, F.; Sorace, L.; Sainctavit, P.; Arrio, M.-A.; Otero, E.; Joly, L.; Cezar, J.C.; et al. Quantum tunnelling of the magnetization in a monolayer of oriented single-molecule magnets. *Nature* **2010**, *468*, 417–421. [CrossRef]
7. Mannini, M.; Pineider, F.; Sainctavit, P.; Danieli, C.; Otero, E.; Sciancalepore, C.; Talarico, A.M.; Arrio, M.-A.; Cornia, A.; Gatteschi, D.; et al. Magnetic memory of a single-molecule quantum magnet wired to a gold surface. *Nat. Mater.* **2009**, *8*, 194–197. [CrossRef]
8. Malavolti, L.; Lanzilotto, V.; Ninova, S.; Poggini, L.; Cimatti, I.; Cortigiani, B.; Margheriti, L.; Chiappe, D.; Otero, E.; Sainctavit, P.; et al. Magnetic bistability in a submonolayer of sublimated Fe_4 single-molecule magnets. *Nano Lett.* **2015**, *15*, 535–541. [CrossRef]
9. Cornia, A.; Mannini, M.; Sessoli, R.; Gatteschi, D. Propeller-Shaped Fe_4 and Fe_3M Molecular Nanomagnets: A Journey from Crystals to Addressable Single Molecules. *Eur. J. Inorg. Chem.* **2019**, *2019*, 552–568. [CrossRef]
10. Erler, P.; Schmitt, P.; Barth, N.; Irmler, A.; Bouvron, S.; Huhn, T.; Groth, U.; Pauly, F.; Gragnaniello, L.; Fonin, M. Highly ordered surface self-assembly of Fe_4 single molecule magnets. *Nano Lett.* **2015**, *15*, 4546–4552. [CrossRef]
11. Paschke, F.; Erler, P.; Enenkel, V.; Gragnaniello, L.; Fonin, M. Bulk-Like Magnetic Signature of Individual Fe_4H Molecular Magnets on Graphene. *ACS Nano* **2019**, *13*, 780–785. [CrossRef]
12. Gragnaniello, L.; Paschke, F.; Erler, P.; Schmitt, P.; Barth, N.; Simon, S.; Brune, H.; Rusponi, S.; Fonin, M. Uniaxial 2D Superlattice of Fe_4 Molecular Magnets on Graphene. *Nano Lett.* **2017**, *17*, 7177–7182. [CrossRef] [PubMed]
13. Serrano, G.; Poggini, L.; Briganti, M.; Sorrentino, A.L.; Cucinotta, G.; Malavolti, L.; Cortigiani, B.; Otero, E.; Sainctavit, P.; Loth, S.; et al. Quantum dynamics of a single molecule magnet on superconducting Pb(111). *Nat. Mater.* **2020**, *19*, 546–551. [CrossRef]
14. Barra, A.-L.; Bianchi, F.; Caneschi, A.; Cornia, A.; Gatteschi, D.; Gorini, L.; Gregoli, L.; Maffini, M.; Parenti, F.; Sessoli, R.; et al. New single-molecule magnets by site-specific substitution: Incorporation of "alligator clips" into Fe_4 complexes. *Eur. J. Inorg. Chem.* **2007**, 4145–4152. [CrossRef]
15. Kappler, J.-P.; Otero, E.; Li, W.; Joly, L.; Schmerber, G.; Muller, B.; Scheurer, F.; Leduc, F.; Gobaut, B.; Poggini, L.; et al. Ultralow-temperature device dedicated to soft X-ray magnetic circular dichroism experiments. *J. Synchrotron Radiat.* **2018**, *25*, 1727–1735. [CrossRef]
16. Cornia, A.; Barra, A.-L.; Poneti, G.; Tancini, E.; Sessoli, R. Unbiased evaluation of zero-field splitting D parameter in high-spin molecules from DC magnetic data with incomplete powder averaging. *J. Magn. Magn. Mater.* **2020**, *510*, 166713. [CrossRef]
17. Cini, A.; Mannini, M.; Totti, F.; Fittipaldi, M.; Spina, G.; Chumakov, A.; Rüffer, R.; Cornia, A.; Sessoli, R. Mössbauer spectroscopy of a monolayer of single molecule magnets. *Nat. Commun.* **2018**, *9*, 480. [CrossRef]

18. Totaro, P.; Poggini, L.; Favre, A.; Mannini, M.; Sainctavit, P.; Cornia, A.; Magnani, A.; Sessoli, R. Tetrairon(III) single-molecule magnet monolayers on gold: Insights from ToF-SIMS and isotopic labeling. *Langmuir* **2014**, *30*, 8645–8649. [CrossRef]
19. Rodriguez-Douton, M.J.; Mannini, M.; Armelao, L.; Barra, A.-L.; Tancini, E.; Sessoli, R.; Cornia, A. One-step covalent grafting of Fe_4 single-molecule magnet monolayers on gold. *Chem. Commun.* **2011**, *47*, 1467–1469. [CrossRef]
20. Rodriguez-Douton, M.J.; Sessoli, R.; Cornia, A. A novel tripodal ligand with organosulfur alligator clips for deposition of tetrairon(III) single-molecule magnets on gold. *Polyhedron* **2011**, *30*, 2960–2964. [CrossRef]
21. Ciszek, J.W.; Stewart, M.P.; Tour, J.M. Spontaneous Assembly of Organic Thiocyanates on Gold Sufaces. Alternative Precursors for Gold Thiolate Assemblies. *J. Am. Chem. Soc.* **2004**, *126*, 13172–13173. [CrossRef]
22. Ciszek, J.W.; Keane, Z.K.; Cheng, L.; Stewart, M.P.; Yu, L.H.; Natelson, D.; Tour, J.M. Neutral Complexes of First Row Transition Metals Bearing Unbound Thiocyanates and Their Assembly on Metallic Surfaces. *J. Am. Chem. Soc.* **2006**, *128*, 3179–3189. [CrossRef] [PubMed]
23. Béthencourt, M.I.; Srisombat, L.; Chinwangso, P.; Lee, T.R. SAMs on Gold Derived from the Direct Adsorption of Alkanethioacetates Are Inferior to Those Derived from the Direct Adsorption of Alkanethiols. *Langmuir* **2009**, *25*, 1265–1271. [CrossRef] [PubMed]
24. Lau, K.H.A.; Huang, C.; Yakovlev, N.; Chen, Z.K.; O'Shea, S.J. Direct Adsorption and Monolayer Self-Assembly of Acetyl-Protected Dithiols. *Langmuir* **2006**, *22*, 2968–2971. [CrossRef] [PubMed]
25. Vaughan, O.P.H.; Turner, M.; Williams, F.J.; Hille, A.; Sanders, J.K.M.; Lambert, R.M. Direct Observation of Surface-Mediated Thioacetyl Deprotection: Covalent Tethering of a Thiol-Terminated Porphyrin to the Ag(100) Surface. *J. Am. Chem. Soc.* **2006**, *128*, 9578–9579. [CrossRef]
26. Biebuyck, H.A.; Bain, C.D.; Whitesides, G.M. Comparison of Organic Monolayers on Polycrystalline Gold Spontaneously Assembled from Solutions Containing Dialkyl Disulfides or Alkanethiols. *Langmuir* **1994**, *10*, 1825–1831. [CrossRef]
27. Biebuyck, H.A.; Whitesides, G.M. Interchange between monolayers on gold formed from unsymmetrical disulfides and solutions of thiols: Evidence for sulfur-sulfur bond cleavage by gold metal. *Langmuir* **1993**, *9*, 1766–1770. [CrossRef]
28. Tollens, B.; Wiegand, P. Über den Penta-Erythrit, einen aus Formaldehyd und Acetaldehyd synthetisch hergestellten vierwerthigen Alkohol. *Liebigs Ann. der Chemie* **1891**, *265*, 316–340. [CrossRef]
29. Dermer, O.C.; Solomon, P.W. Extensions of the Tollens Condensation. *J. Am. Chem. Soc.* **1954**, *76*, 1697–1699. [CrossRef]
30. Tancini, E.; Mannini, M.; Sainctavit, P.; Otero, E.; Sessoli, R.; Cornia, A. On-Surface Magnetometry: The Evaluation of Superexchange Coupling Constants in Surface-Wired Single-Molecule Magnets. *Chem. Eur. J.* **2013**, *19*, 16902–16905. [CrossRef]
31. Singh, R.; Whitesides, G.M. Comparisons of rate constants for thiolate-disulfide interchange in water and in polar aprotic solvents using dynamic ^{1}H NMR line shape analysis. *J. Am. Chem. Soc.* **1990**, *112*, 1190–1197. [CrossRef]
32. Lothian-Tomalia, M.K.; Hedstrand, D.M.; Tomalia, D.A.; Padias, A.B.; Hall, H.K. A contemporary survey of covalent connectivity and complexity. The divergent synthesis of poly(thioether) dendrimers. Amplified, genealogically directed synthesis leading to the de Gennes dense packed state. *Tetrahedron* **1997**, *53*, 15495–15513. [CrossRef]
33. Stellenboom, N.; Hunter, R.; Caira, M.R. One-pot synthesis of unsymmetrical disulfides using 1-chlorobenzotriazole as oxidant: Interception of the sulfenyl chloride intermediate. *Tetrahedron* **2010**, *66*, 3228–3241. [CrossRef]
34. Mukaiyama, T.; Takahashi, K. A convenient method for the preparation of unsymmetrical disulfides by the use of diethyl azodicarboxylate. *Tetrahedron Lett.* **1968**, *9*, 5907–5908. [CrossRef]
35. Le Coustumer, G.; Catel, J.-M. Synthese Et Etude Electrochimique De Disulfures Thiopheniques. *Phosphorus. Sulfur. Silicon Relat. Elem.* **2006**, *181*, 191–217. [CrossRef]
36. Duchenet, V.; Andrieu, C.G.; Catel, J.-M.; Le Coustumer, G.; Penneau, J.-F.; Le Guillanton, G.; Hapiot, P.; Audebert, P. Thienyl and thenyl alkyl disulfides: Monomers and polymers. *J. Chim. Phys. Physico Chimie Biol.* **1998**, *95*, 1229–1233. [CrossRef]

37. Accorsi, S.; Barra, A.-L.; Caneschi, A.; Chastanet, G.; Cornia, A.; Fabretti, A.C.; Gatteschi, D.; Mortalò, C.; Olivieri, E.; Parenti, F.; et al. Tuning anisotropy barriers in a family of tetrairon(III) single-molecule magnets with an S = 5 ground state. *J. Am. Chem. Soc.* **2006**, *128*, 4742–4755. [CrossRef]
38. Gregoli, L.; Danieli, C.; Barra, A.-L.; Neugebauer, P.; Pellegrino, G.; Poneti, G.; Sessoli, R.; Cornia, A. Magnetostructural correlations in tetrairon(III) single-molecule magnets. *Chem. Eur. J.* **2009**, *15*, 6456–6467. [CrossRef]
39. Lunghi, A.; Totti, F. DFT magnetic characterization of a Fe_4 SMMs series: From isotropic exchange interactions to multi-spin zero field splitting. *J. Mater. Chem. C* **2014**, *2*, 8333–8343. [CrossRef]
40. Cole, K.S.; Cole, R.H. Dispersion and Absorption in Dielectrics I. Alternating Current Characteristics. *J. Chem. Phys.* **1941**, *9*, 341–351. [CrossRef]
41. Dekker, C.; Arts, A.F.M.; de Wijn, H.W.; van Duyneveldt, A.J.; Mydosh, J.A. Activated dynamics in a two-dimensional Ising spin glass: $Rb_2Cu_{1-x}Co_xF_4$. *Phys. Rev. B* **1989**, *40*, 11243–11251. [CrossRef]
42. Prasad, T.K.; Poneti, G.; Sorace, L.; Rodriguez-Douton, M.J.; Barra, A.-L.; Neugebauer, P.; Costantino, L.; Sessoli, R.; Cornia, A. Magnetic and optical bistability in tetrairon(III) single molecule magnets functionalized with azobenzene groups. *Dalton Trans.* **2012**, *41*, 8368–8378. [CrossRef]
43. Rodriguez-Douton, M.J.; Cornia, A.; Sessoli, R.; Sorace, L.; Barra, A.-L. Introduction of ester and amido functions in tetrairon(III) single-molecule magnets: Synthesis and physical characterization. *Dalton Trans.* **2010**, *39*, 5851–5859. [CrossRef]
44. Armarego, W.L.F.; Chai, C.L.L. *Purification of Laboratory Chemicals*, 5th ed.; Butterworth-Heinemann: Burlington, VT, USA, 2003; ISBN 0-7506-7571-3.
45. Issidorides, C.H.; Matar, A.I. Pentaerythritol Derivatives. I. The Preparation of Pentaerythritol Monomethyl Ether. *J. Am. Chem. Soc.* **1955**, *77*, 6382–6383. [CrossRef]
46. Ishizone, T.; Tominaga, T.; Kitamura, K.; Hirao, A.; Nakahama, S. Protection and Polymerization of Functional Monomers. 25. Synthesis of Well-Defined Polystyrene Bearing a Triol Functionality by Means of Anionic Living Polymerization of 4-[(4-(4-Vinylphenyl)butoxy)methyl]-1-methyl-2,6,7-trioxabicyclo[2.2.2]octane. *Macromolecules* **1995**, *28*, 4829–4836. [CrossRef]
47. Fulmer, G.R.; Miller, A.J.M.; Sherden, N.H.; Gottlieb, H.E.; Nudelman, A.; Stoltz, B.M.; Bercaw, J.E.; Goldberg, K.I. NMR Chemical Shifts of Trace Impurities: Common Laboratory Solvents, Organics, and Gases in Deuterated Solvents Relevant to the Organometallic Chemist. *Organometallics* **2010**, *29*, 2176–2179. [CrossRef]
48. Altomare, A.; Cascarano, G.; Giacovazzo, C.; Guagliardi, A. Completion and refinement of crystal structures with SIR92. *J. Appl. Crystallogr.* **1993**, *26*, 343–350. [CrossRef]
49. Sheldrick, G.M. Crystal structure refinement with SHELXL. *Acta Crystallogr. Sect. C Struct. Chem.* **2015**, *71*, 3–8. [CrossRef]
50. Farrugia, L.J. WinGX and ORTEP for Windows: An update. *J. Appl. Crystallogr.* **2012**, *45*, 849–854. [CrossRef]
51. Thorn, A.; Dittrich, B.; Sheldrick, G.M. Enhanced rigid-bond restraints. *Acta Crystallogr. Sect. A Found. Crystallogr.* **2012**, *68*, 448–451. [CrossRef]
52. *Persistence of Vision Raytracer*; Version 3.5; Persistence of Vision Pty. Ltd.: Williamstown, Victoria, Australia, 2002.
53. Bain, G.A.; Berry, J.F. Diamagnetic Corrections and Pascal's Constants. *J. Chem. Educ.* **2008**, *85*, 532–536. [CrossRef]
54. *E04FCF, E04YCF and F02ABF, NAG Fortran Library Routines (Mark 17)*; NAG Ltd.: Oxford, UK, 1996.
55. Jacobsen, C.J.H.; Pedersen, E.; Villadsen, J.; Weihe, H. ESR characterization of trans-$V^{II}(py)_4X_2$ and trans-$Mn^{II}(py)_4X_2$ (X = NCS, Cl, Br, I; py = pyridine). *Inorg. Chem.* **1993**, *32*, 1216–1221. [CrossRef]
56. Mossin, S.; Weihe, H.; Barra, A.-L. Is the Axial Zero-Field Splitting Parameter of Tetragonally Elongated High-Spin Manganese(III) Complexes Always Negative? *J. Am. Chem. Soc.* **2002**, *124*, 8764–8765. [CrossRef] [PubMed]

Publisher's Note: MDPI stays neutral with regard to jurisdictional claims in published maps and institutional affiliations.

© 2020 by the authors. Licensee MDPI, Basel, Switzerland. This article is an open access article distributed under the terms and conditions of the Creative Commons Attribution (CC BY) license (http://creativecommons.org/licenses/by/4.0/).